

Discovery of an Extreme AGN-mode Feedback on 100 kpc Scale at $z=2.3$ in an Enormous Ly α Nebula

Abstract

Galaxy feedback now appears as an attractive mechanism to resolve some of the outstanding problems with the modern cosmological model. outflows powered by starburst or AGN have been reported to extend to tens of kiloparsecs. However, these observations mainly focus on low redshifts and rare feedback at high redshifts, especially the peak epoch of star formation, is observed. Here we report integral field unit (IFU) observation targeting on a famous enormous Ly α nebula around BOSS1441 at $z \approx 2.3$ with Keck Cosmic Web Imager (KCWI). We find widely effected outflow ejected from MAMMOTH-1 extends to 100 kpc with extended HeII and CIV emissions reaching to 80 kpc and H α emission reaching to 120 kpc. By fitting the Spectral Energy Distribution (SED) of BOSS1441 and comparing it with radio galaxies we confirm that it is a radio-quiet quasar. The velocity offset between blueshifted and redshifted line emission approximates to 1000 km/s and FWHM of Ly α emission is beyond 1400 km/s. We also estimate the outflow energy rate $\dot{E}_{\text{out}} \approx 3 \times 10^{45}$ erg/s which is relatively high comparing to other observations. These evidences show that this outflow is extremely violent and powerful. By comparing the extended scale and coupling efficiency with simulation prediction, we find only AGN-mode feedback can interpret our observation. This result may put a strong constrain on theory of AGN feedback and help us to further understand its role in the coevolution process of galaxies and their environments.

Key words: Galaxies – Enormous Ly α Nebula – AGN feedback – outflow

1. Introduction

Over the past few decades it has been realized that the black hole (BH) at the centre of a galaxy bulge is more than just decorations but plays a key role in galaxy evolution (Fabian 2012). This process is known as Active Galactic Nucleus (AGN) feedback which takes place by accreting matter onto the massive BH and have a profound effect on galaxy evolution even the large-scale structure comparing with the large ratio of the size of BH to host galaxy. For example, the energy released to build a BH with mass $M_{\text{BH}} = 10^8 M_{\odot}$ would correspond to $E_{\text{BH}} \approx 0.1 M_{\text{BH}} c^2$. This total accretion energy is two-to-three order of magnitude higher than the binding energy of the galaxy bulge the BH reside in, and is comparable to, even higher than, the thermal energy of the gas in the dark matter halo (Harrison 2016). As a consequence, feedback induced by massive BH has the ability to change the evolution path of galaxies. Observations are required to constrain the details of when, where and how these processes actually occur.

There are two sorts of AGN feedback mechanisms. The first one is the radio mode feedback also known as maintenance mode or kinetic mode, it is believed that this mode is the most efficient mechanism in low redshift clusters, at late times and during periods of low BH accretion rates. The objects that are responsible for this type of feedback are likely

to be low-excitation radio AGN which has low accretion rate and are always companied by radio lobes (Churazov et al. 2005; Bower et al. 2006; McCarthy et al. 2011). This sort of feedback is mainly used to explain the cut-off of the galaxy luminosity function in cluster environment (Bower et al. 2006; Croton et al. 2006; Somerville et al. 2008). In addition, a more powerful form of interaction between AGN and its environment happens during periods of rapid accretion known as quasar mode or radiative mode. Objects which is responsible for this type of feedback are the radiatively-efficient AGN possessing large accretion rate. Theoretical models for this form of feedback typically require $\approx 0.005 - 0.15$ of the accretion energy to couple to the cold gas within the host galaxy and to expel this gas through outflows which ultimately results in the shut-down of future BH growth or star formation (Benson et al. 2003; Hopkins & Beacom 2006; DeBuhr et al. 2012). Besides, analytical models have used the idea of galaxy-scale outflows initially launched by AGN, to explain $M_{\text{BH}} - M_{\text{bulge}}$ relationship (Fabian 1999; Granato et al. 2004; King et al. 2011; Faucher-Giguère & Quataert 2012). This form of feedback is thought to be effective at producing high mass outflow rates and quenching star formation. In addition to the potential affects of AGN feedback described above, AGN-driven outflows are required to blow the gas in their host galaxy out to explain the chemical enrichment of intercluster medium (ICM) and circumgalactic medium (CGM) (Borgani et al. 2008; Wiersma et al. 2009; Fabjan et al. 2010; Ciotti et al. 2010). In contrast, it has been

prompted that, these outflows could induce positive feedback which trigger star formation by inducing pressure in cold gas reservoirs (Nayakshin & Zubovas 2012; Ishibashi & Fabian 2012; Silk 2013). However, there are still many fundamental questions to be solved, it is not well established how the accretion energy couples to the gas to drive outflows and the impact of outflow on a much larger physical scale.

Spectroscopy is used as a direct way to search for outflows. Such observations have identified outflows in ionized, atomic and molecular gas (Nesvadba *et al.* 2008). A method that is widely used to search for outflowing ionized gas is the high-velocity OIII λ 5007 emission line. This is a good tracer of kinematics in the narrow-line region (NLR) of AGN and people have used it to study kinematics in hundreds to ten of thousands of AGN (Wang *et al.* 2011; Mullaney *et al.* 2013) to constrain the ubiquity of these outflow features and study them as a function of key AGN properties. However, These studies have used only one-dimensional spectra and therefore provide no insight on the spatial extent or structure of the outflows. Even for long-slit spectroscopy only spectrum of light passing through the slit is obtained. In contrast, the spatial information is crucial to study the outflow, such as the sphere of influence, kinematic energy and momentum. These kinds of information help us to understand how feedback influence the evolution of host galaxy, furthermore, how it change the large-scale kinematics environment. The spatial resolved emission (absorption)-line profile may provide information about how feedback change the chemical environment of ICM and CGM and constrain the theoretical models. Hence, Integral field spectroscopy (IFS) is required for these studies. Harrison *et al.* (2014) used integral field unit (IFU) observations covering OIII λ 4959, 5007 and H β emission lines to study the outflows of 16 type-2 AGN at $z < 0.2$. They found high-velocity ionized gas with observed spatial extents of 6-16 kpc. Their study demonstrates that galaxy-wide energetic outflows are not confined to the most extreme star-forming galaxies or radio-luminous AGN. In another observation, Rupke *et al.* (2019) shows optical integral field observations of the low-redshift galaxy SDSS J211824.06+001729.4 with Keck Cosmic Web Imager (KCWI), the OII lines at wavelengths of 3726 and 3729 angstroms reveal an ionized outflow spanning 80 by 100 square kiloparsecs.

Comparing with low-redshift observation, observation for high-redshift outflow is insufficient in contrast to how dramatic galaxy evolution at this epoch. Several pieces of observational evidence suggest that the most violent galaxy evolution occurred at high redshift ($z \approx 1 - 3$). Firstly, the cosmic space density of BH growth peaks at $z \approx 1 - 2$ while over half of the integrated BH growth occurred around these redshift (Schmidt & Green 1983; Richards *et al.* 2006). Secondly, the peak density of the most intensely star-forming galaxies is at $z \approx 2$ (Chapman *et al.* 2005; Wardlow *et al.* 2011), with the peak in cosmic star formation density occurring at the same stage (Madau *et al.* 1996; Lilly *et al.* 1999; Madau & Dickinson 2014). Studies of local galaxies have also suggested that massive galaxies formed the bulk of their stars at high red-

shift ($z \geq 1 - 2$). In conclusion, this is an essential stage for galaxy evolution, observation of the universal outflow at this epoch is crucial to reveal how galaxies co-evolve with their environments.

Motivated by the above reasons, in this paper we report a follow-up observation on the famous overdensity field centering on BOSS1441 with KCWI. This is a cluster core at $z \approx 2.3$ known as MAMMOTH-1 which was found in Cai *et al.* (2017b). It is shown that BOSS1441 has an Ly α emitter (LAE) overdensity $\delta \approx 10$. The follow-up narrow band (NB) imaging with Mayall-4 m telescope reveals a widely extended enormous Ly α nebula (ELAN) with projected scale ≥ 400 kpc around BOSS1441 (Cai *et al.* 2017b). These works reveal that a large reservoir of cool Ly α emitting gas can exist in the core of a cluster at $z > 2$. Nevertheless, the warm gas content (10^5 K) in the $z > 2$ cluster environment is not probed yet. In contrast to observation, The nature of the powering mechanism of this nebula is still unclear. In Section 2 we give details of IFU observations and data preprocessing. In Section 3 we present the results and model used to estimate outflow energy In Section 4 we discuss the Ly α nebula and the possible mechanism to power the strong outflow. Finally we give a brief summary in Section 5. Throughout this paper, we assume a flat cosmological model with $\omega_\Lambda = 0.7, \omega_m = 0.3$ and $H_0 = 70$ km/s/Mpc. In this cosmology, $1'' \approx 8.2$ kpc at $z = 2.3$.

2. Observations

2.1. KCWI Instrument Configuration

In this section, we provide details on the observation and KCWI instrument configurations. We obtained IFU spectroscopy of BOSS1441 on UT-20180518 with KCWI on Keck-II. The large slicer, with Field of View (FoV) of $20'' \times 33''$, was employed for this observation which has the spatial resolution of $\approx 1.35''$. We choose this slicer because it possesses the largest FoV to cover MAMMOTH-1 as widely as possible. We also employed blue BL1 grating centered at $\lambda = 4500$ Å, which gives a usable wavelength coverage of $3500 - 5600$ Å, and is an excellent regime to perform studies of Ly α nebula at $z \approx 2.3$. This configuration yields a slit-limited spectral resolution of $R \approx 1000$ (rest-frame 300 km/s) which is high enough to fully resolve the kinematics of MAMMOTH-1. The total on-source exposure time is 4 hours conducted with two pointings, we integrated for 2 hours consisting of 6 exposures of 20 min for each pointing. This exposure time allows us to reach a surface brightness equals to 7×10^{-19} erg s $^{-1}$ cm $^{-2}$ arcsec $^{-2}$. We didn't apply nod-and-shuffle, instead we interleaved observation for a nearby patch of sky ($\Delta RA = +2', \Delta DEC = +1'$) for 4 hours to later perform sky subtraction, a standard star was also observed for flux calibration purposes.

2.2. Data Reduction

The data was reduced using the XXX pipeline. In this process, we first subtracted bias, corrected the variation by dividing the flat-field images from each raw image, removed

cosmic-rays and created error images. Then we did geometric transformation and wavelength calibration. Finally we calibrated flux for each image with the spectrophotometric standard star. With all of these done, σ clipping was performed for each sky cube by masking pixels with value 3σ above the median, then we used the masked cube to estimate the sky channel-by-channel and subtracted it from the reduced data cube.

2.3. 3D mask construction

The final step is to construct the three-dimensional segmentation mask (3D mask) in order to obtain the low-dimensional projections of the extracted sources, such as optimally-extracted images and flux-weighted-moment map, for further analysis. We produce the 3D mask based on the user-defined signal-to-noise ratio (SNR) threshold, pixels in data cube with value lower than the threshold are masked which means the value of the corresponding pixels in 3D mask is 0, otherwise 1. Because this process is based on the SNR threshold, the estimation of the background noise is an essential aspect. This noise is estimated under the assumption that background noise of each wavelength layer in the data cube shares the same value. This assumption allows us to calculate the standard deviation with parts of the data cube which don't contain the emission and absorption components and apply it to the whole data cube. The SNR threshold is set to be 2σ which typically corresponds to a flux density of $10^{-18} \text{ erg s}^{-1} \text{ cm}^{-2} \text{ \AA}^{-1}$.

After this preliminary work, we find widely extended HeII and CIV emission and an extremely powerful outflow reaching hundreds of kiloparsec which is never seen before at high redshift. In Sec. 3 we show our results to confirm this outflow and in Sec. 4 we give detailed discussion.

3. Results

3.1. Radio Emission

Emonts et al. (2019) used sensitive low-surface-brightness observations of Very Large Array (VLA) to trace the cold molecular gas in the inner region of MAMMOTH-1 by detecting the CO (1-0) emission. They found four CO sources which are a few kpc away from the associated galaxies or groups. This result suggests that the core of the potential well of this Ly α nebula is marked by the cold gas rather than the obscured AGN. Since none of the continuum image (center on 35 GHz and 150 GHz) from VLA and Atacama Large Millimeter/submillimeter Array (ALMA) shows significant signal, we use them to give a $3\text{-}\sigma$ upper limit on its continuum emission in radio band, $f_{35, \text{up}} = 0.050 \text{ mJy}$, $f_{150, \text{up}} = 0.066 \text{ mJy}$. By combining these two upper limits with the optical and infrared data from Arrigoni Battaia et al. (2018a), we fit the spectral energy distribution (SED) of BOSS1441 with M82 template from Silva et al. (1998) in Fig.1. Gray lines represent the SEDs of "radio-excess" galaxies in Harrison et al. (2014) with triangles representing the flux density at 1.4 GHz (rest frame) of these sources. The purple points are the flux of MRC 1138-262 which is also known as spider galaxy with extreme radio emission at $z=2.16$ (Nesvadba

et al. 2006). The brown dashed line is the average of SEDs belonging to 1056 radio galaxies (RG) with redshifts in the range of 0.0028 – 1.7 (Toba et al. 2019). All of these SEDs and data have been normalized and shifted to $z = 2.31$. M82 template fits extremely well with flux of source-B even including the two upper limits from ALMA and VLA, this evidence suggests that source-B should be a star burst galaxy. In addition, the departure of flux of source-B and M82 template from RG template and flux of spider galaxy indicates that there is no strong radio emission from source-B caused by AGN activity.

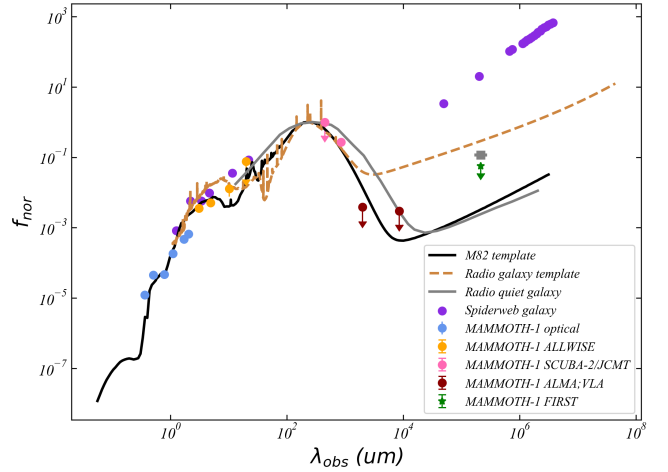


Figure 1: SED for source-B powering ELAN MAMMOTH-1. The data points are from Cai et al. (2017b) (blue), ALLWISE source catalog, SCUBA-2 data (Arrigoni Battaia et al. 2018a) (magenta), ALMA and VLA continuum images (Emonts et al. 2019) (dark red) and FIRST catalog (green). Gray lines and points are SEDs and flux density at 1.4 GHz for radio excess galaxies from Harrison et al. (2014). The brown dashed line is the average template of 1056 radio galaxies at redshifts from 0.0028 to 1.7 (Toba et al. 2019). All of this data are normalized and shifted to $z=2.3$.

We calculate the ratio (q_{IR}) between the far-infrared (8 – 1000 μm) and radio emission with the definition given by Ivison et al. (2010) to quantitatively decide if source-B has significant radio emission, this ratio is usually used to identify if there is significant radio emission above that expected from their star-formation activity (radio emission results from AGN or other process). The formula is given by:

$$q_{\text{IR}} = \log \left[\frac{S_{\text{IR}} / 3.75 \times 10^{12} \text{ W m}^{-2}}{S_{1.4} / \text{W m}^{-2} \text{ Hz}^{-1}} \right] \quad (1)$$

where S_{IR} is the rest-frame flux in far-infrared range (8 – 1000 μm) and $S_{1.4}$ is the flux density at 1.4 GHz in rest frame. Arrigoni Battaia et al. (2018a) performed a follow-up observation for MAMMOTH-1 to constrain the SED with the available data and derived some properties of source-B. The far-infrared luminosity is integrated from this SED $L_{\text{IR}} = 3.2 \times 10^{12} L_{\odot}$. Through setting the luminosity distance to be

$D_L = 18773.8$ Mpc at redshift $z=2.3$, it is easy to calculate the far-infrared flux $S_{IR} = 2.9 \times 10^{-16}$ W cm $^{-2}$. Because the D-configuration of VLA doesn't cover $\nu_{obs} = 0.42$ GHz (1.4 GHz in rest frame), we adopt $S_{1.4}=0.01$ mJy from M82 SED template. We note here that the constrain of continuum, $f_{150,up}$, is one-order-magnitude lower than that of M82 SED template, therefore the true flux density at $\nu_{rest} = 1.4$ GHz is possibly lower than 0.01 mJy. By adopting $S_{1.4} = 0.01$ mJy the low limit of q_{IR} is equal to 1.9. Ivison et al. (2010) and Del Moro et al. (2013) define "radio excess" sources as those with $q_{IR} \leq 1.8$, this calculation also supports that source-B has no significant radio emission.

Based on these evidences we conclude that source-B is most likely a radio-quiet quasar with no strong radio emission due to AGN activity.

3.2. Morphology and Emission

We construct continuum-free line images by summing over the wavelength range of the emission lines in data cubes and subtracting the underlying continuum component from them. The continuum component is estimated by taking average from another wavelength range out of line emission (or absorption). We show the results in the left panel of Fig. ???. The three contours of different colors representing signal-to-noise ratio (SNR) show the spatially extended emission of Ly α HeII and CIV with the first contour corresponding to 2 and steps between contours to 2. The background image was taken by Wide Field Camera 3 (WFC3) on Hubble Space Telescope (HST) with F160W filter. Sources labeled from G-1 to G-5 are galaxies at the same redshift ($z \approx 2.3$) with Source-B confirmed by CO (1-0) emission and CO (3-2) emission (Emonts et al. 2019; Li et al. 2020). The emitting structure shows Ly α nebula covers all of the marked objects and extends to 20'' which corresponds to 164 kpc. It also shows that the physical projected size of extended HeII and CIV emission reaches to 9'' corresponding to 74 kpc.

Spectra are extracted within aperture centering on the peak of emission with radius of 1.5'' (larger than the spatial resolution of KCWI) and shown in the right panel. To determine the redshifts of these widely extended nebulae, we fit the three emission lines with one-component gaussian function and estimate the wavelength of line centre. The fitted parameters are shown in Tab.1. By converting the line width (Å) to FWHM (km/s) it seems that all of the three emission line have a relatively large FWHM which equals to $FWHM_{Ly} = 1225$ km/s, $FWHM_{HeII} = 1039$ km/s and $FWHM_{CIV} = 1786$ km/s. This result indicates that there may be extremely violent kinematic activity in the nebula on a physical scale of 100 kpc.

Because the surface brightness (SB) values for both kinematically narrow and broad features would have been either lost in the noise or underestimated in a narrow-band (NB) image with single width of wavelength, we adopt optimally-extract method from Borisova et al. (2016) to construct psudo-NB images which can reach to a larger dynamic range comparing to a standard image. These images are obtained by using a three dimensional segmentation mask

(3D mask) which defines a three-dimensional SNR surface in the cube, pixels with values below the SNR threshold are masked and only pixels possessing significant signal are extracted. Therefore, the signal of each pixel are integrated along a slightly different range in wavelength which allows us to obtain images or spectra with maximal SNR after stacking along spatial axis or spectral axis. In particular, images presented in Fig. ?? (left column) are obtained by using this method after continuum-subtraction and stacking along spectral axis. The three extended emissions are detected at faint levels with 1- σ SB of $SB_{Ly} = xxx \text{ erg s}^{-1} \text{ cm}^{-2} \text{ arcsec}^{-2}$, $SB_{HeII} = xxx \text{ erg s}^{-1} \text{ cm}^{-2} \text{ arcsec}^{-2}$ and $SB_{CIV} = xxx \text{ erg s}^{-1} \text{ cm}^{-2} \text{ arcsec}^{-2}$.

We also obtain the NB image of H α emission with MOIRCS on Subaru Telescope by using the BrG filter centering on 2.165 μm . Leibler et al. (2018) suggests the ratio between Ly α emission and H α emission $\frac{F_{Ly\alpha}}{F_{H\alpha}}$ can be used as an indicator of the powering mechanism of the nebula. So, we calculate the ratio map of H α comparing to Ly α and show it in Fig. ??. The total flux of H α emission is $7.67 \pm 0.89 \times 10^{-16} \text{ erg s}^{-1} \text{ cm}^{-2}$, by applying the Ly α flux from Cai et al. (2017b), the ratio is $\frac{F_{Ly\alpha}}{F_{H\alpha}} = 15.60 \pm 0.12$. This result relatively large than the expected value of photoionization recombination radiation may indicates that there is another mechanism playing a significant role. The H α emission is also shown to extend to 116 kpc which is comparable with the Ly α emission observed by KCWI. Plus the extended HeII and CIV emission, MAMMOTH-1 is supposed to be the very unique source at $z \approx 2$.

	$\lambda_c(\text{\AA})$	$\sigma_\lambda(\text{\AA})$	L(erg/s)	redshift
Ly α	4024	7	2.68×10^{44}	2.310
HeII	5438	8	1.97×10^{43}	2.316
CIV	5143	13	2.29×10^{43}	2.320

Table 1:

3.3. Kinematics

In this section we present the maps for flux-weighted velocity and flux-weighted dispersion of Ly α , HeII and CIV emissions produced with the 3D mask to get an indication of kinematic patterns. We note that Ly α resonant scattering effect doesn't play an important role on kinematics seen in the central area because it tends to disrupt the coherency of kinematics instead of enhancing it (Cantalupo et al. 2005), this is also confirmed by the results of HeII and CIV emissions.

Fig. ?? shows the two moment maps together with the optimally-extracted images of the three emissions. The optimally-extracted images in left panel clearly shows the projected physical scale of Ly α emission extends to 175 kpc which approximates the typical size of dark matter halo at this redshift. This projected scale is smaller comparing to the results of Cai et al. (2017b) due to small FoV (20'' \times 33'')

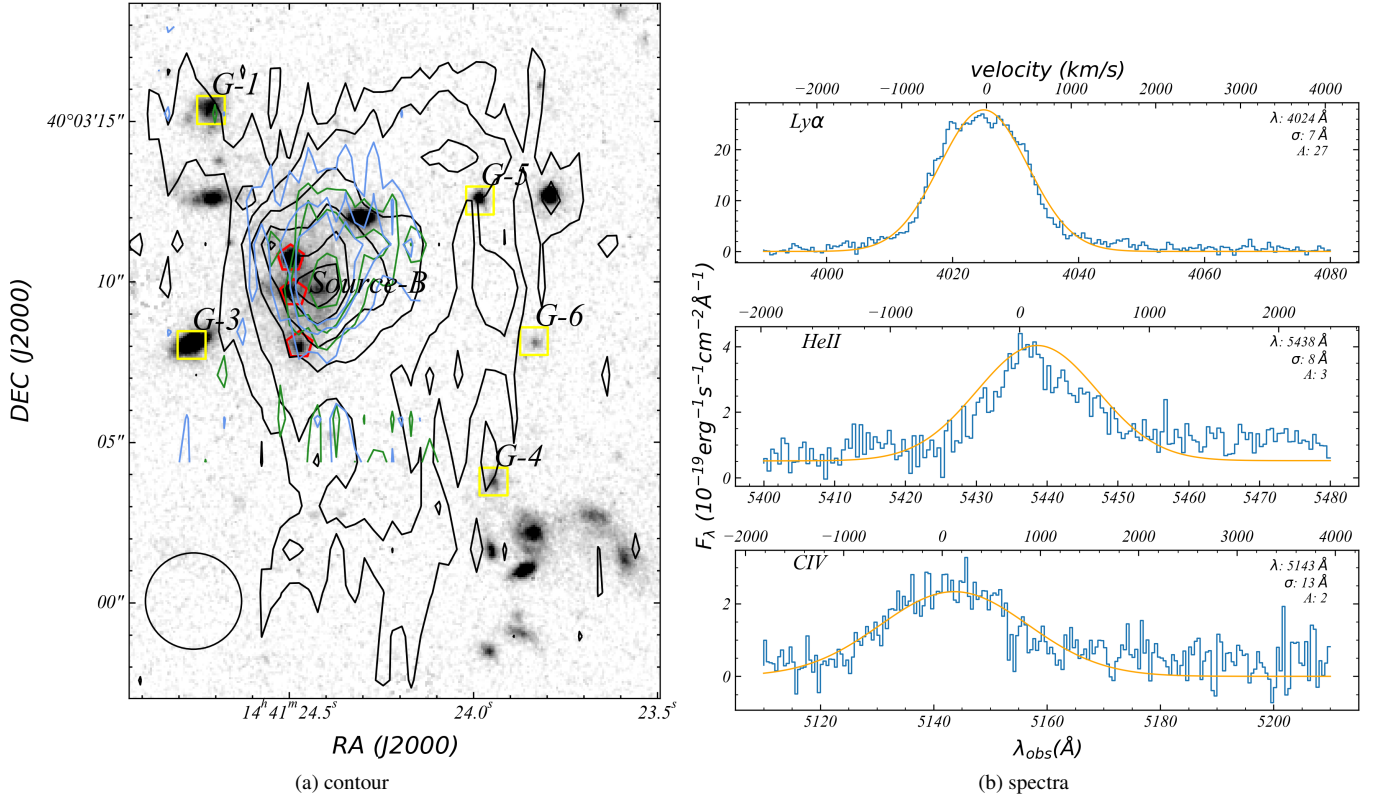


Figure 2: Left: HST image of MAMMOTH-1 from circle 24,25, PI: Cai. We overlay on it Ly α HeII and CIV pseudo narrow band images. Black contour is Ly α , blue contour is HeII, green contour is CIV. We also mark source-B with red mark and sources at the same redshift with yellow mark. We also plot circle with radius of 1 arcsec^2 . Right: spectra of the 3 emission lines extracted from aperture center on source-B with radius 1 arcsec^2 , we fit them with one-component gaussian function.

of KCWI. In addition, HeII and CIV emission also extends to tens of kiloparsec surpassing the typical size of galaxies, especially CIV emission which extends to 88 kpc. This spatially widely extended metal emissions are rarely seen at high redshift with such large projected scale.

In the middle and right panel we present the maps of first and second moment of flux distribution. The middle panel represents the flux-weighted centroid velocity maps, it shows that the velocity gradients are evident in the three maps with same direction from the northwest to the southeast. This kinematic pattern is usually the indication of rotating gas disk in CGM or outflow ejected from central AGN. Besides, the velocity map of Ly α emission also shows gradient around G-5 from northeast to southwest. The velocity dispersion map of Ly α emission shows that the area around source-B possesses larger velocity dispersion ($\sigma_v > 400 \text{ km/s}$) and extends to 100 kpc, dispersion even larger than 650 km/s which corresponds to FWHM of 1550 km/s in some spatial positions. Following the same method in Arrigoni Battaia et al. (2018) the expected velocity dispersion calculated for a dark matter halo hosting quasars is 300 km/s with the results $M_{\text{DM}} \approx 10^{13} M_\odot$ in Cai et al. (2017b) where M_{DM} is the mass of dark matter halo. The significant comparison between expected dispersion and our results may indicate that there is extremely powerful kinematic activity in this region which is impossibly caused by rotation or inflow.

Fig. ?? shows the channel map of Ly α emission with step of 200 km/s. It is clearly seen that the red component and blue component are on either side of source-B. Besides, We also extract the spectra which are normalized and fitted with one-component gaussian function of different spatial positions from circular aperture with radius of $1.5''$ and show it in Fig. ?. No significant symmetric doublets existing in the spectra confirms that the resonant scattering effect is negligible.

Based on the above analysis, we rule out the possibility that the kinematic pattern is result from rotating gas disk, inflow and resonant scattering effect of Ly α emission. Together with the existing of extended HeII CIV and OIII emission (Cai et al. 2017b), the most natural and straightforward interpretation is that there is extremely powerful and widely influenced outflow ejected from source-B which has the ability to influence the entire gas environment in dark matter halo hosting source-B. The large-scale feedback effect has been widely reported before, however these observations mainly focus on the central galaxies of low redshift clusters and they are mostly powered by jet with significant radio signal. So, the halo-scale-influenced outflow with no strong radio signal at high redshift makes our observation extremely unique. As a consequence, understanding the mechanism powering this strong outflow in our observation is essential for feedback effect on galaxy evolution.

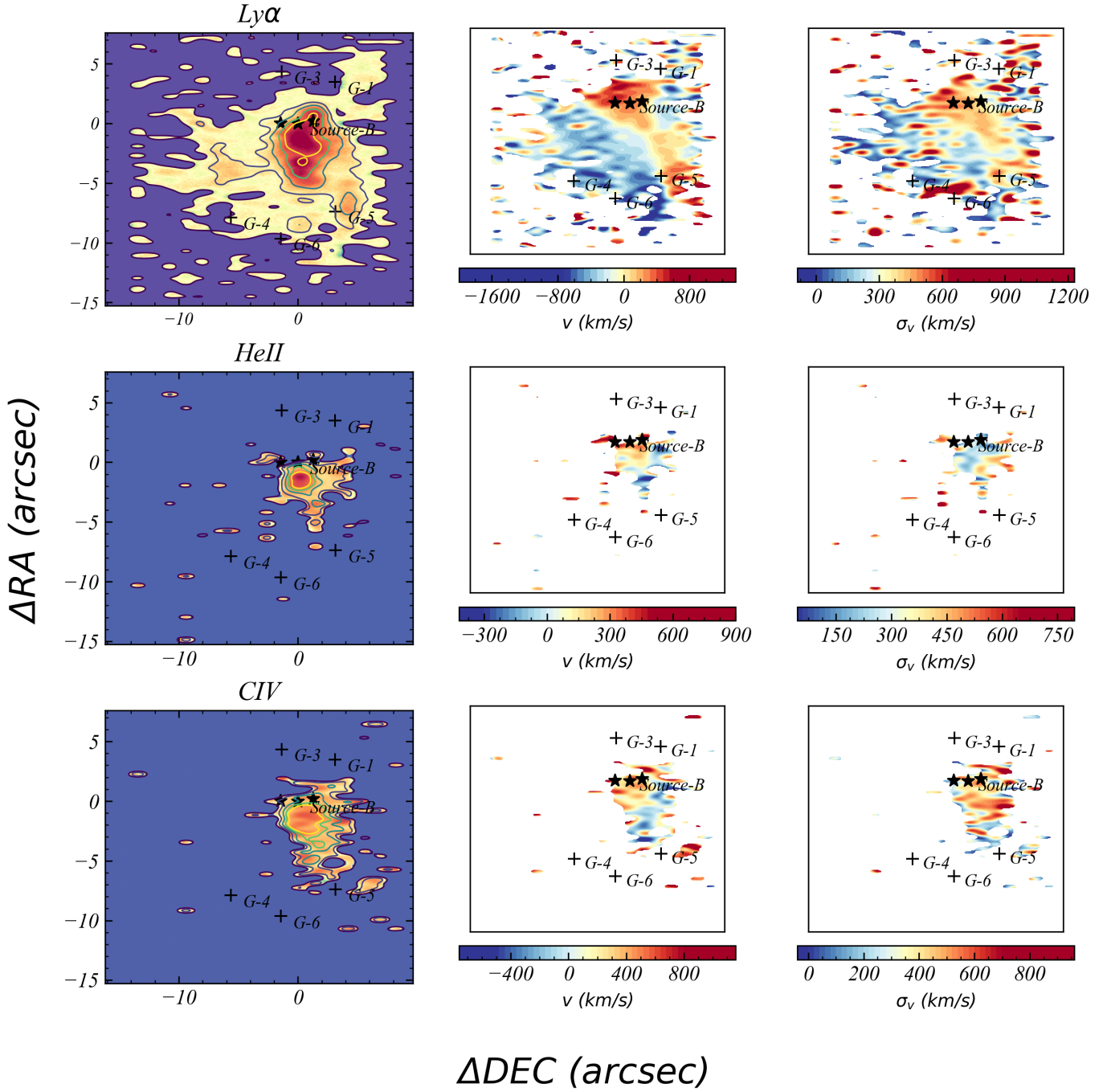


Figure 3: Left: continuum-subtracted pseudo-narrow band images for the 3 emissions. We select regions $> 1.5\sigma$ in each slice and stack these slices together. The contour represent signal-to-noise ratio(SNR), for $Ly\alpha$ is (5 σ , 9 σ , 18 σ , 30 σ , 42 σ , 51 σ), for $HeII$ is (3 σ , 5 σ , 9 σ) and for CIV is (4 σ , 7 σ , 9 σ). Middle: flux-weighted velocity map with respect to the systemic redshift of MAMMOTH-1. Right: flux-weighted velocity dispersion also with respect to systemic redshift of MAMMOTH-1. We also mark sources in the field with cross.

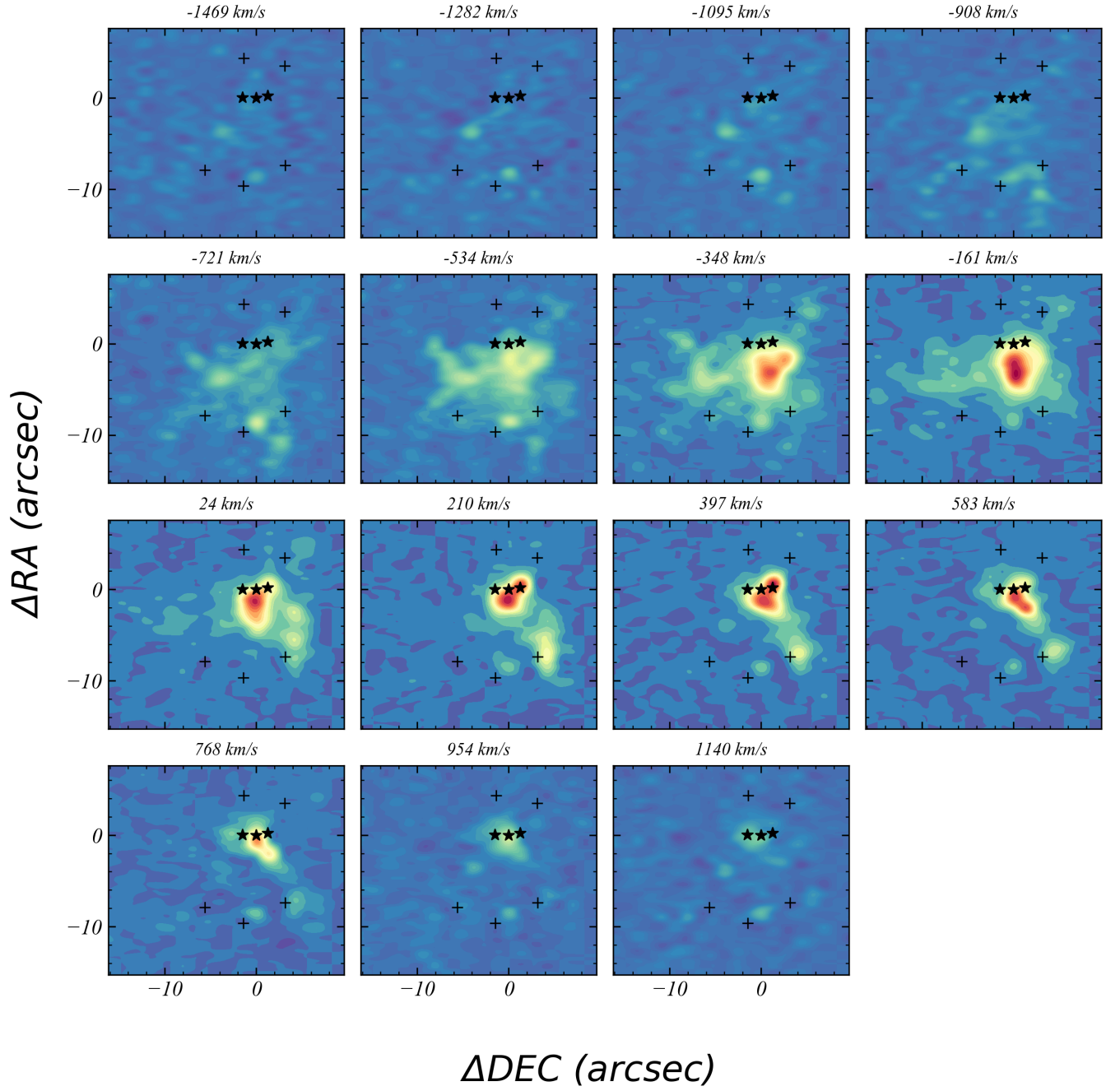


Figure 4: Kinematics of cool gas. It shows signal of $\text{Ly}\alpha$ emission at different velocities. We select $\Delta v = 187 \text{ km/s}$ which corresponds 4\AA as the bin size of these slices. We extract these slices within the range $4000\text{\AA} - 4040\text{\AA}$, for each image here, we use the mean velocity of the bin as title for each image. It shows significant red and blue component on either side of source-B.

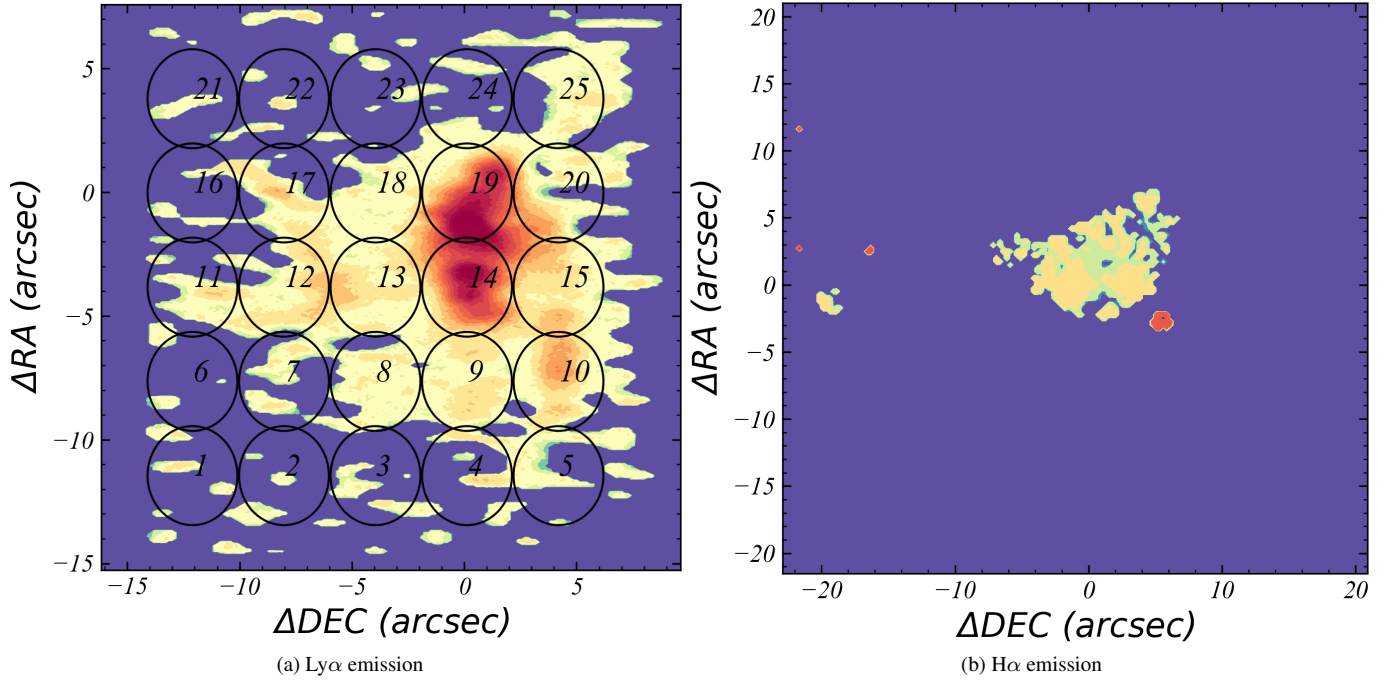


Figure 5: Left: Continuum-subtracted pseudo narrow band image of Ly α . We overlay circles on it and number them from 1 to 25.

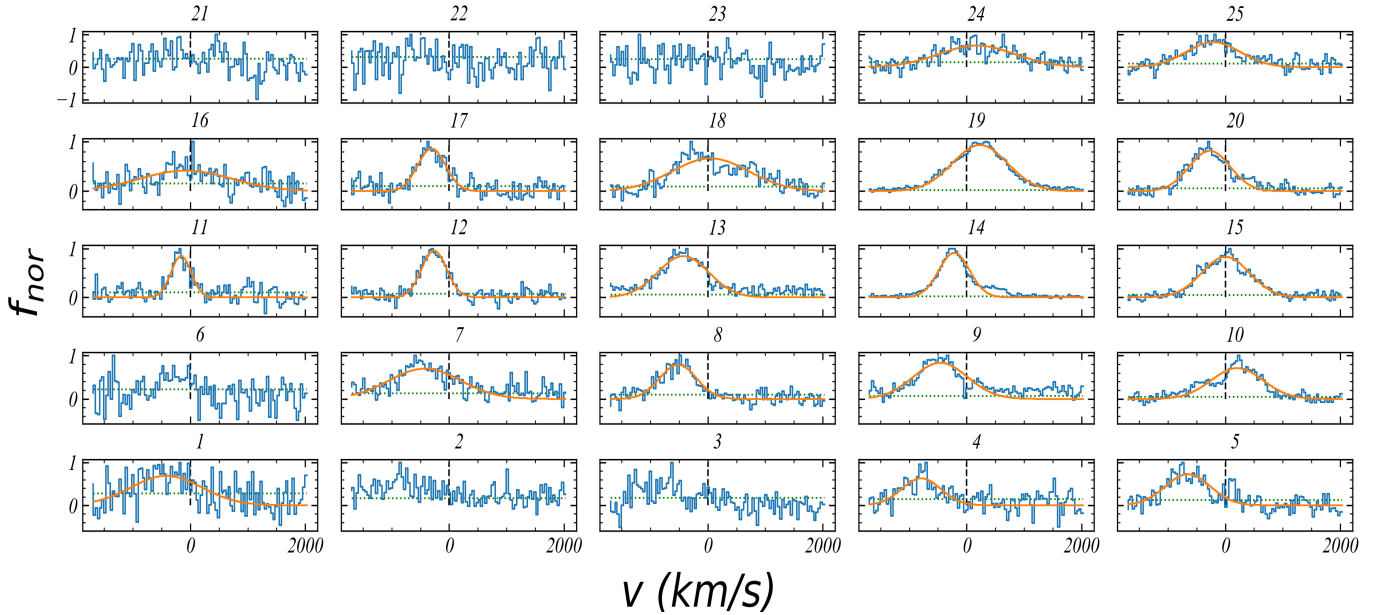


Figure 6: Continuum-subtracted spectra extracted from individual spatial regions indicated in upper panel. The apertures are circle with radius of 2arcsec^2 . We number the spectra from 1 to 25 which corresponds to circles in upper panel. We fit the emission line with single gaussian function and show it with orange lines. The green lines show the noise level calculated from the high-frequency component of spectra.

3.4. Model of the outflow

The mass rate, energy rate and momentum rate being carried by outflow are important to help us understand the physical mechanisms to drive the outflow. Although outflow are likely to be entraining gas in multiphases, the cool and warm gas observed here could represent a large fraction of the overall mass and energy of the total outflows. Because of the complication of modeling outflows, here we adopt simple outflow models to provide first order constraints. Following the same process of Harrison et al. (2014), the outflow energy rate is estimated with two methods which give the upper limit and low limit respectively. We calculate the mean value of these limits in logarithmic space and use it as the fiducial value. The low limit is given by Eq.7 of Rodriguez Zaun et al. (2013):

$$\dot{M} = \frac{3Lm_p v_{\text{out}}}{\alpha_{\text{Ly}\alpha}^{\text{eff}} h\nu_{\text{Ly}\alpha} n_e r} \quad (2)$$

where L is the luminosity of $\text{Ly}\alpha$ emission, m_p is the proton mass, v_{out} is outflow velocity, $\alpha_{\text{Ly}\alpha}^{\text{eff}}$ is recombination coefficients which is obtained from Storey & Hummer (1995), $h\nu_{\text{Ly}\alpha}$ is the energy of $\text{Ly}\alpha$ photons, n_e is electron density and r is the radius of the outflow to its host, we adopt $r = 30$ kpc for our case. The kinetic power of the outflow \dot{E} relating to the velocity dispersion, mass outflow rate and outflow velocity is also given by Rodriguez Zaun et al. (2013):

$$\dot{E} = \frac{\dot{M}}{2} (v_{\text{out}}^2 + 3\sigma^2) \quad (3)$$

the main uncertainty in calculating the mass outflow rates is electron density which is often measured from the emission-line ratio $\text{SII } \lambda 6716/\lambda 6731$. Because this doublet is not covered by our IFU observations, we adopt the value $n_e = 1.25 \text{ cm}^{-3}$ from Cai et al. (2017b). With the above equations and values, we obtain $\dot{M}_{\text{out,low}} \approx 500 M_{\odot} \text{ yr}^{-1}$. With the velocity dispersion $\sigma_v = 600 \text{ km/s}$, we derive the energy outflow rate to be $\dot{E}_{\text{out,low}} \approx 10^{44} \text{ erg/s}$.

To estimate the upper limit, we calculate the mass energy injection rates by assuming an energy conserving bubble in a uniform medium (Heckman et al. 1990) which gives the relation:

$$\dot{E}_{\text{out,up}} \approx 1.5 \times 10^{46} r_{10}^2 v_{1000}^3 n_{0.5} \text{ erg/s} \quad (4)$$

where r_{10} is the radius in unit of 10 kpc, v_{1000} in unit of 1000 km/s and $n_{0.5}$ is in unit of 0.5 cm^{-3} . Using this method we obtain $\dot{E}_{\text{out,up}} \approx 9 \times 10^{46} \text{ erg/s}$. The mass outflow rate is then given by $\dot{M}_{\text{out,up}} = 2\dot{E}_{\text{out,up}}/c^2$ where c is the speed of light, this gives $\dot{M}_{\text{out,up}} \approx 8.7 \times 10^5 M_{\odot} \text{ yr}^{-1}$. So the fiducial value is $\dot{E}_{\text{out,mean}} = 3 \times 10^{45} \text{ erg/s}$.

In preparation for the follow discussion, we also estimate outflow momentum rate by taking the mass outflow rate calculated above and assuming $\dot{P}_{\text{out}} = \dot{M}_{\text{out}} v_{\text{out}}$.

4. Discussion

4.1. What drives the outflow?

In this section we will investigate which of these processes could be responsible for driving the extreme outflows observed. The dominant processes that drive such large scale outflow in protocluster and the efficiency to which they are able to couple the gas are currently sources of uncertainty in galaxy formation models. Several possible mechanisms have been suggested to drive galaxy-wide outflows, for example: the stellar wind and supernovae; radiation pressure from the extremely luminous AGN or star formation; the interaction of radio jets with a clumpy and multiphase interstellar medium; AGN wind initially launched from the accretion disc. Following Harrison et al. (2014), we calculate the coupling efficiency which is a popular method to investigate the likely drivers of large-scale outflow. We compare the ratio of our outflow kinetic energy rate (\dot{E}_{out}) with (1) the AGN bolometric luminosity converted from AGN IR luminosity; (2) the star formation luminosity (Arrighi Battaia et al. 2018a). We also calculate the momentum-loading factor for both star-forming-driven case and AGN-driven case. Using these results we now explore the possible driving mechanisms to power this outflow.

Fig.?? shows coupling efficiency for both star-forming-driven case and AGN-driven case. We compare our result with results in Harrison et al. (2014). One way for star formation to drive large-scale outflow is by stellar winds or supernovae. An estimation of the coupling efficiency for this case is carried by Kennicutt Jr (1998), he found that the maximum coupling efficiency is $\dot{E}_{\text{out}}/L_{\text{IR,SF}} \approx 0.02$, we indicate this upper limit with gray dot line in Fig.?. Based on this result, stellar winds and supernovae are unlikely to be fully responsible to power outflow on physical scale of 100 kpc. By adopting a potential model for a halo with stellar mass $M_* = 3 \times 10^{11} M_{\odot}$ at $z \approx 2$ we run stellar feedback simulation, it shows the initial outflow velocity should reach 2300 km/s to meet our observation. However, neither of Heckman & Borthakur (2016) nor Li & Bryan (2020) shows stellar feedback can power such large initial velocity which also indicates stellar formation is not a good interpretation for our case. On the other hand, the coupling efficiency for AGN-driven case is too large which is close to 1. In the right panel of Fig.? it shows that if the outflow is driven by AGN, it has already exceed other results with similar AGN luminosity.

Besides, if we instead consider a momentum-driven wind with momentum deposition from the radiation pressure of stars or AGN, the momentum loading factors are $f_{p,\text{SF}} = 1.7$ and $f_{p,\text{AGN}} = 3.2$ for the two mechanisms. Nevertheless Zubovas (2018) suggests that a typical momentum loading factor for star-formation-driven case is $f_{p,\text{SF}} < 1.4$ which is lower than our estimation, this comparison also rules out the star-formation case. In the same way, we also find that $f_{p,\text{AGN}}$ is larger than the typical value.

Moreover, Shankar et al. (2006) mentions the two sources of feedback have different effects over different mass ranges, in particular, stellar feedback regulates the processes in low-

Number	1	4	5	7	8	9	10	11	12	13	14	15	16	17	18	19	20	24	25
Velocity(km/s)	-416	-785	-649	-419	-515	-453	208	-157	-257	-424	-211	9	-75	-300	49	236	-267	182	-208
Dispersion(km/s)	618	342	392	626	319	474	450	174	219	444	269	415	799	242	668	481	358	660	472
f_{norm}	0.69	0.63	0.73	0.70	0.79	0.83	0.71	0.84	0.95	0.85	0.91	0.83	0.41	0.86	0.66	0.93	0.81	0.66	0.77

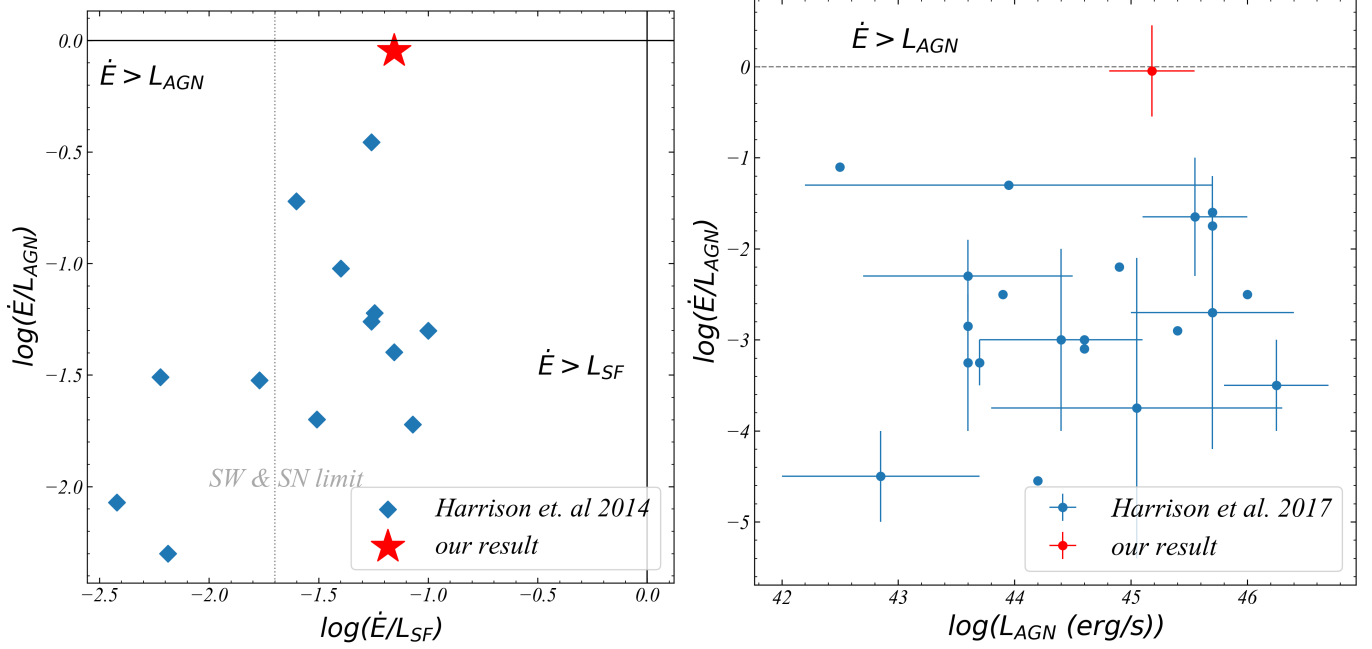


Figure 7: Left: the ratio of our estimated outflow kinetic energy rates (E_{out}) to the AGN luminosity and to the star formation luminosity for our source (red) and sources from Harrison et al. (2014). The dashed vertical line is the estimated maximum mechanical input expected from supernovae and stellar winds. The two solid lines show the coupling efficiency of 1. Right: Observationally determined kinetic coupling efficiencies in Harrison et al. (2018) and our result. The vertical lines show the range of values quoted or, in the case of an error bar, the quoted error on the average value. The horizontal lines show the range of bolometric luminosity for each sample. The dotted line shows coupling efficiency of 1.

mass galaxies while large galaxies are mainly regulated by AGN feedback. The transition mass for these two feedback mechanisms is $M_{tr} \approx 2 \times 10^{10} M_{\odot}$. By fitting the SED of source-B, Arrigoni Battaia et al. (2018b) estimates its stellar mass of source-B to be $\log(M_{star}/M_{\odot}) = 11.4^{+0.3}_{-0.2}$. Comparing with M_{tr} , it also confirms star-forming driven feedback is not the possible mechanism to power this outflow.

However, Zubovas (2018) also suggests there are mechanisms to reach high coupling efficiency and momentum loading factor. One possibility is hyper-Eddington Super Massive Black Hole (SMBH) growth during Compton-thick (heavily obscured) phase. In this case, SMBH would accrete material with extremely large rate and may lead to ultra fast outflows (UFO). Tombesi et al. (2013) shows the initial velocity is able to reach to $0.1c$ and will have a strong coupling with the interstellar medium (ISM). Fig. 6 of Tombesi et al. (2013) shows the coupling efficiencies approximate 1 for some cases, but he also explains that this extremely fast and powerful outflow would occur only very close to SMBH $R \approx 100r_s$ (where r_s is the Schwarzschild radius.). He indicates that the large coupling efficiency is probably due to large envi-

ronment column density $\approx 10^{24} \text{ cm}^{-2}$ and highly ionized state which is similar to the large-scale environmental conditions of MAMMOTH-1. Cai et al. (2017b) suggests that the hydrogen column density is in the range 10^{20} cm^{-2} , with the presence of highly-coupling outflow we indicate here that the column density in CGM may be 10^3 cm^{-2} larger than this value.

In summary, based on above analyses we find MAMMOTH-1 outflow is likely to be powered by AGN wind during the hyper-Eddington accretion of SMBH instead of star-forming processes. Although there is large uncertainty in the estimation of coupling efficiency, the very-large-scale-effecting feedback is never observed before. If it is true, our result should be the first observation of AGN-mode feedback on 100 kpc. It puts a very strong constrain on galaxies feedback processes and even further affects our understanding of galaxy evolution.

4.2. Galaxies merger

By fitting the SED and estimating IR luminosity, Arrigoni Battaia et al. (2018a) suggests source-B is an Ultra-

Luminous Infrared Galaxy (ULIRG). Some substantial observational evidences indicate that ULIRGs (heavily obscured galaxies) are the product from the gas-rich merger of two massive galaxies (Treister et al. 2010). Cai et al. (2017a) demonstrates BOSS1441 is a protocluster in an extremely dense environment with overdensity reaching to $\sigma = 10.8 \pm 2.6$. The HST imaging further confirms this result by imaging eight galaxies within 200 kpc. These evidences suggests this region is under galaxies merger process.

We suggest that the physical picture of this area is like this: three sources of source-B is experiencing galaxy merger, the center source accretes gas and material from the other two sources to supply its SMBH for rapid growth and meanwhile producing strong outflow. Owing to the tidal effect between the three sources, lots of material is pulled out from galaxies which causes the dense gas environment. This can also explain why there's such large coupling efficiency between outflow and environment. In addition, from the velocity and dispersion map we see that the region with large dispersion extent to G-5 and there's also obvious velocity gradient on either side of G-5. This clue may indicate that there is likely outflow from G-5 also.

4.3. Emission mechanism

Cantalupo (2017) demonstrates there are three physical processes that are able to produce extended and bright Ly α emission. The first is the recombination radiation following hydrogen photoionization, the second is Ly α scattering of photons produced by a nearby star forming galaxy or quasar, and the last is Ly α collisional excitation and recombination radiation following collisional ionization. Leibler et al. (2018) shows that the expected integrated $\frac{F_{\text{Ly}\alpha}}{F_{\text{H}\alpha}}$ ratio for photoionization recombination should range between 8.1-11.6 which is lower than our result. Our measured value of $\frac{F_{\text{Ly}\alpha}}{F_{\text{H}\alpha}} = 15.60 \pm 0.12$ satisfies Ly α scattering process which requires this ratio larger than 12, however plenty of neutral hydrogen, column density of which larger than 10^{21}cm^{-2} (Cantalupo 2017) is also necessary to produce the emission. So collisional excitation and recombination radiation is the most possible process to dominant the nebula here due to the widely effected outflow powering by AGN. In addition, because the BOSS1441 seems to be a star burst quasar it should possess strong UV emission which can also contribute to the extreme Ly α emission.

5. Conclusions

In this paper, we present the Keck/KCWI IFU observation of ELAN in protocluster at $z \approx 2.3$ found by Cai et al. (2017a). With KCWI we discover an extremely powerful outflow from BOSS1441 influencing the halo environment up to 100 kpc. The extended HeII emission together with CIV emission up to 80 kpc are never reported before. By comparing its SED with that of radio galaxies, we confirm BOSS1441 is a radio-quiet quasar with no significant radio emission due to jet or AGN. The kinematical map obtained from the three emission lines shows the the velocity offset of the outflow is 1000 km/s with FWHM > 1400 km/s.

By comparing the kinematical results and coupling efficiency with simulations, we suggest this outflow is powered by AGN wind launched from the disc of SMBH. This is the first time observing the influence of AGN mode feedback on CGM scale and will help us to further understand the coevolution of galaxies with its surrounding gas environments.

References

- Arrigoni Battaia, F. et al. 2018a, *Astronomy & astrophysics.*, 620, A202
- Arrigoni Battaia, F., Hennawi, J. F., Prochaska, J. X., Oñorbe, J., Farina, E. P., Cantalupo, S., & Lusso, E. 2018b, *Monthly Notices of the Royal Astronomical Society*, 482, 3162
- Arrigoni Battaia, F., Hennawi, J. F., Prochaska, J. X., Oñorbe, J., Farina, E. P., Cantalupo, S., & Lusso, E. 2018, *Monthly Notices of the Royal Astronomical Society*, 482, 3162–3205
- Benson, A., Bower, R., Frenk, C., Lacey, C. G., Baugh, C., & Cole, S. 2003, *The Astrophysical Journal*, 599, 38
- Borgani, S., Fabjan, D., Tornatore, L., Schindler, S., Dolag, K., & Diaferio, A. 2008, *Space Science Reviews*, 134, 379
- Borisova, E. et al. 2016, *The Astrophysical Journal*, 831, 39
- Bower, R. G., Benson, A., Malbon, R., Helly, J., Frenk, C., Baugh, C., Cole, S., & Lacey, C. G. 2006, *Monthly Notices of the Royal Astronomical Society*, 370, 645
- Cai, Z. et al. 2017a, *The Astrophysical Journal*, 839, 131
- Cai, Z. et al. 2017b, *The Astrophysical Journal*, 837, 71
- Cantalupo, S. 2017, *Astrophysics and Space Science Library*, 195–220
- Cantalupo, S., Porciani, C., Lilly, S. J., & Miniati, F. 2005, *Astrophysical Journal*, 628, pags. 61
- Chapman, S. C., Blain, A., Smail, I., & Ivison, R. 2005, *The Astrophysical Journal*, 622, 772
- Churazov, E., Sazonov, S., Sunyaev, R., Forman, W., Jones, C., & Böhringer, H. 2005, *Monthly Notices of the Royal Astronomical Society: Letters*, 363, L91
- Ciotti, L., Ostriker, J. P., & Proga, D. 2010, *The Astrophysical Journal*, 717, 708
- Croton, D. J. et al. 2006, *Monthly Notices of the Royal Astronomical Society*, 365, 11
- DeBuhr, J., Quataert, E., & Ma, C.-P. 2012, *Monthly Notices of the Royal Astronomical Society*, 420, 2221
- Del Moro, A. et al. 2013, *Astronomy & Astrophysics*, 549, A59
- Emonts, B. H., Cai, Z., Prochaska, J. X., Li, Q., & Lehnert, M. D. 2019, *The Astrophysical Journal*, 887, 86
- Fabian, A. 1999, *Monthly Notices of the Royal Astronomical Society*, 308, L39
- Fabian, A. 2012, *Observational evidence of AGN feedback*
- Fabjan, D., Borgani, S., Tornatore, L., Saro, A., Murante, G., & Dolag, K. 2010, *Monthly Notices of the Royal Astronomical Society*, 401, 1670
- Faucher-Giguère, C.-A., & Quataert, E. 2012, *Monthly Notices of the Royal Astronomical Society*, 425, 605
- Granato, G. L., De Zotti, G., Silva, L., Bressan, A., & Danese, L. 2004, *The Astrophysical Journal*, 600, 580
- Harrison, C., Alexander, D., Mullaney, J., & Swinbank, A. 2014, *Monthly Notices of the Royal Astronomical Society*, 441, 3306
- Harrison, C., Costa, T., Tadhunter, C., Flütsch, A., Kakkad, D., Perna, M., & Vietri, G. 2018, *Nature Astronomy*, 2, 198
- Harrison, C. M. 2016, *Observational constraints on the influence of active galactic nuclei on the evolution of galaxies* (Springer)
- Heckman, T. M., Armus, L., Miley, G. K., et al. 1990, *Astrophysical Journal Supplement Series*, 74, 833
- Heckman, T. M., & Borthakur, S. 2016, *Astrophysical Journal*, 822, 9

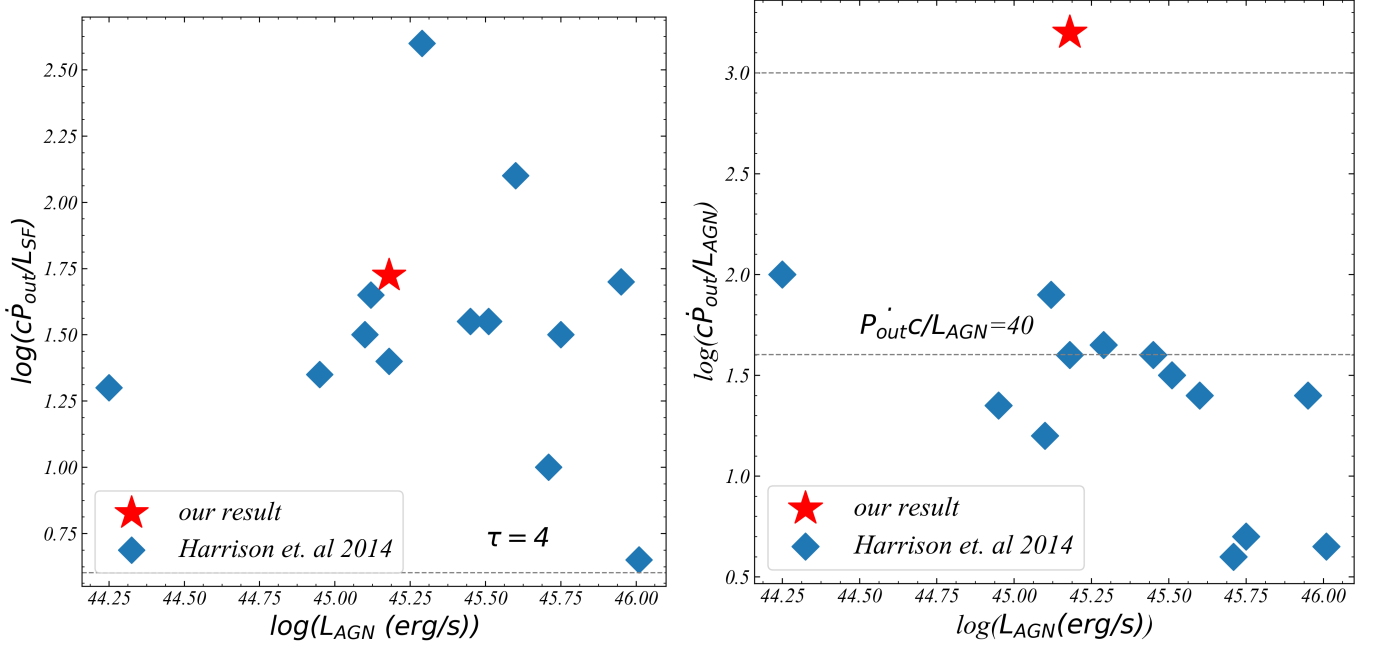


Figure 8: Left: momentum rates of the outflows (\dot{P}_{out} normalized to the star formation luminosity L_{SF}/c) versus AGN luminosity. The dashed lines represent the required optical depths if the outflows are driven by radiation pressure from star formation. Right: momentum rate of outflows normalized to AGN luminosity (L_{AGN}/c) versus AGN luminosity. Based on our assumptions, the outflows are unlikely to be purely radiatively driven, the ratio is also too high for theoretical predictions of energy-driven outflows launched by AGN accretion-disc wind.

Hopkins, A. M., & Beacom, J. F. 2006, *The Astrophysical Journal*, 651, 142
 Ishibashi, W., & Fabian, A. 2012, *Monthly Notices of the Royal Astronomical Society*, 427, 2998
 Ivison, R. et al. 2010, *Astronomy & Astrophysics*, 518, L31
 Kennicutt Jr, R. C. 1998, *Annual Review of Astronomy and Astrophysics*, 36, 189
 King, A., Zubovas, K., & Power, C. 2011, *Monthly Notices of the Royal Astronomical Society: Letters*, 415, L6
 Leibler, C. N., Cantalupo, S., Holden, B. P., & Madau, P. 2018, *Monthly Notices of the Royal Astronomical Society*, 480, 2094–2108
 Li, M., & Bryan, G. L. 2020, *The Astrophysical Journal*, 890, L30
 Li, Q., aa, c., & bb, d. 2020, in prep
 Lilly, S. J., Eales, S. A., Gear, W. K., Hammer, F., Le Fèvre, O., Crampton, D., Bond, J. R., & Dunne, L. 1999, *The Astrophysical Journal*, 518, 641
 Madau, P., & Dickinson, M. 2014, *Annual Review of Astronomy and Astrophysics*, 52, 415
 Madau, P., Ferguson, H. C., Dickinson, M. E., Giavalisco, M., Steidel, C. C., & Fruchter, A. 1996, *Monthly Notices of the Royal Astronomical Society*, 283, 1388
 McCarthy, I. G., Schaye, J., Bower, R. G., Ponman, T. J., Booth, C. M., Vecchia, C. D., & Springel, V. 2011, *Monthly Notices of the Royal Astronomical Society*, 412, 1965
 Mullaney, J., Alexander, D., Fine, S., Goulding, A., Harrison, C., & Hickox, R. 2013, *Monthly Notices of the Royal Astronomical Society*, 433, 622
 Nayakshin, S., & Zubovas, K. 2012, *Monthly Notices of the Royal Astronomical Society*, 427, 372
 Nesvadba, N., Lehnert, M., De Breuck, C., Gilbert, A., & Van Breugel, W. 2008, *Astronomy & Astrophysics*, 491, 407
 Nesvadba, N. P. H., Lehnert, M. D., Eisenhauer, F., Gilbert, A., Tecza, M., & Abuter, R. 2006, *The Astrophysical Journal*, 650, 693–705

Richards, G. T. et al. 2006, *The Astronomical Journal*, 131, 2766
 Rodriguez Zaurin, J., Tadhunter, C., Rose, M., & Holt, J. 2013, *Monthly Notices of the Royal Astronomical Society*, 432, 138
 Rupke, D. S. et al. 2019, *Nature*, 574, 643
 Schmidt, M., & Green, R. 1983, *The Astrophysical Journal*, 269, 352
 Shankar, F., Lapi, A., Salucci, P., De Zotti, G., & Danese, L. 2006, *The Astrophysical Journal*, 643, 14
 Silk, J. 2013, *The Astrophysical Journal*, 772, 112
 Silva, L., Granato, G. L., Bressan, A., & Danese, L. 1998, *The Astrophysical Journal*, 509, 103
 Somerville, R. S., Hopkins, P. F., Cox, T. J., Robertson, B. E., & Hernquist, L. 2008, *Monthly Notices of the Royal Astronomical Society*, 391, 481
 Storey, P., & Hummer, D. 1995, *Monthly Notices of the Royal Astronomical Society*, 272, 41
 Toba, Y. et al. 2019, *The Astrophysical Journal Supplement Series*, 243, 15
 Tombesi, F., Cappi, M., Reeves, J., Nemmen, R., Braito, V., Gaspari, M., & Reynolds, C. 2013, *Monthly Notices of the Royal Astronomical Society*, 430, 1102
 Treister, E., Natarajan, P., Sanders, D. B., Urry, C. M., Schawinski, K., & Kartaltepe, J. 2010, *Science*, 328, 600
 Wang, J., Mao, Y., & Wei, J. 2011, *The Astrophysical Journal*, 741, 50
 Wardlow, J. L. et al. 2011, *Monthly Notices of the Royal Astronomical Society*, 415, 1479
 Wiersma, R. P., Schaye, J., Theuns, T., Dalla Vecchia, C., & Tornatore, L. 2009, *Monthly Notices of the Royal Astronomical Society*, 399, 574
 Zubovas, K. 2018, *Monthly Notices of the Royal Astronomical Society*, 479, 3189